Process intensification for the synthesis of ultra-small organic nanoparticles with supercritical CO2 in a microfluidic system

Thomas Jaouhari, Fan Zhang, Thierry Tassaing, Suzanne Fery-Forgues, Cyril Aymonier, Samuel Marre, Arnaud Erriguible

Process intensification for the synthesis of ultra-small organic nanoparticles with supercritical CO_2 in a microfluidic system

T. Jaouhari[1], F. Zhang[1], T. Tassaing[2], S. Fery-Forgues[3], C. Aymonier[1], S. Marre[1]*, A. Erriguible[1,4]*

[1]CNRS, Univ. Bordeaux, Bordeaux INP, ICMCB, UMR 5026, F-33600, Pessac Cedex, France
[2]CNRS, Univ. Bordeaux, Bordeaux INP, ISM, F-33405, Talence Cedex, France
[3]SPCMIB, UMR CNRS 5068, Université Toulouse III Paul-Sabatier, 118, route de Narbonne, 31062 Toulouse Cedex 09, France
[4]CNRS, Univ. Bordeaux, Bordeaux INP, I2M, UMR 5295, F-33600, Pessac Cedex, France

ABSTRACT

Submicronization of organic compounds is a challenging requirement for applications in the imaging and pharmaceutical fields. A new Supercritical Anti-Solvent process with microreactor (μSAS) was developed for nanoparticle (NP) synthesis. Tetrahydrofuran (THF) was used to solubilize a model organic molecule, tetraphenylethylene, and supercritical carbon dioxide (sc-CO_2) was used as anti-solvent. The solubility of TPE in the THF/CO_2 system was first measured by *in situ* experiments. Then, NPs of TPE were prepared in various experimental conditions and characterized by transmission electron microscopy (TEM). Chosen experimental conditions led to NPs with a mean size of 9 ± 3 nm. Experimental μSAS results were compared with size distributions obtained by simulation, to obtain surface tension values, which are difficult to access by experiment alone. Simulations coupling Computational Fluid Dynamics (CFD) and Population Balance Equation (PBE) were performed under turbulent conditions in the high pressure microreactors. This coupled experimental and theoretical approaches allowed a deep understanding of the μSAS process and underlined the superior value of this technique for the preparation of NPs.

INTRODUCTION

Putting pure organic dyes and drugs in the form of nanoparticles (NPs) is a very efficient way to enhance their solubility, stability and bioavailability, so that these compounds may find a wide range of applications in the fields of imaging, biosensing and medicine [1–4]. It is therefore critical to develop advanced processes that allow the preparation of small (*i.e.* less than 50 nm) particles with a narrow size distribution. In this view, supercritical fluids (SCFs) processes [5] offer superior performances compared with conventional techniques, *e.g.* milling [6,7] and solvent evaporation [8,9]. Not only the intrinsic properties of SCFs (*i.e.* liquid-like densities and gas-like viscosities) result in high diffusion

coefficients and therefore promote fast mixing, but the operating space is largely extended in terms of pressure and temperature with respect to conventional batch scale processes using liquids. In this context, supercritical carbon dioxide (sc-CO_2) offers distinct advantages for sustainable processes, as it is non-flammable, non-toxic and environmentally friendly. Amongst the myriad of sc-CO_2-based processes, the supercritical antisolvent (SAS) process has been of particular interest for preparing micrometer- [10] and submicrometer-sized [11] particles from various organic materials, such as active pharmaceutical ingredients (APIs) [12] and polymers [13]. The particle morphology and size are affected by experimental parameters like temperature, pressure, molar ratio composition, solution concentration and flow rates, which highlights the importance of the thermo-hydrodynamic phenomena. The general principle consists in mixing a concentrated solution of the compound dissolved in an organic solvent with sc-CO_2, which acts as antisolvent. The solubility of the solute is then dramatically decreased in the final mixture, and this generates high supersaturation, which results in nucleation of the solute. The good solubility of the solute in the organic solvent, its low solubility in sc-CO_2, and the high miscibility of the organic solvent with sc-CO_2 are three essential prerequisites for a successful process. The mixing of the solute solution with sc-CO_2 is a key parameter, because it drives the supersaturating field. Admittedly, a fast mixing leads to a nucleation burst, resulting in small particles with homogeneous size. In most of the SAS set-ups, sc-CO_2 and the solute solution are co-injected into large high-pressure vessels, previously pressurized with sc-CO_2. The particles thus generated are then recovered continuously on a filter. The main limitations of the current approaches are in the limited control of the operating parameters due to the large size of reactors. Sometimes, this leads to poor reproducibility from batch to batch, attributed to the presence of gradients (temperature, concentration, etc.) that directly affects the thermo-hydrodynamics of the system, and therefore the nucleation and growth processes.

In order to intensify the SAS process, it is highly beneficial to use advanced type of reactors, which allow improved control of the operating parameters. Specifically, because they reduce time and space scales, microfluidic systems have shown their effectiveness in controlling mixing and enhancing the performances of materials synthesis processes [14]. The combination of two ways of intensification, SCFs and microfluidic reactors (µSAS), can greatly improve the performance and reproducibility of antisolvent processes, as shown in a previous work for conducting organic polymer nanoparticles [15]. More recently, we have proven that turbulent conditions can be achieved in high pressure microfluidic devices [16], resulting in ultra-fast mixing times down to 10^{-4}-10^{-5} s, highly favorable for synthesizing organic nanoparticles.

In this paper, a coupled numerical/experimental approach was used to explore the µSAS process used for the preparation of organic nanoparticles. Tetraphenylethylene (TPE) is chosen as a polyaromatic and strongly hydrophobic model compound. This molecule is widely used in the aggregated and NP states [17], and advantage will be taken from its particular fluorescence behaviour in a forthcoming work. The synthesis of TPE NPs was achieved with a µSAS process implemented in a

high pressure microreactor, using tetrahydrofuran (THF) and sc-CO_2 as the solvent and antisolvent, respectively. The solubility of TPE in various THF/sc-CO_2 mixtures was first determined. The size of the synthesized NPs and the size distribution were then estimated using transmission electron microscopy (TEM). In parallel, numerical simulation was used to fit the critical parameter of nucleation, *i.e.* the surface tension (σ), from the experimental results. This parameter is very difficult to measure experimentally. The numerical simulation is based on a high performance computing (HPC) massively parallel code, which takes into account all the coupled physical phenomena (*i.e.* thermodynamics, hydrodynamics, nucleation and growth), for catching all the mixing scale [16]. This coupled experimental/numerical approach allows determining the surface tension with a great confidence for two main reasons. First, the good control of the operating conditions in the microchannel reduces the discrepancies between the "ideal" operating conditions of the simulation, and the experimental ones. Secondly, the reactor dimension and the HPC code allow very precise information about hydrodynamics to be obtained. Indeed, all or almost all the mixing length scales are caught, and so we get rid of the uncertainties related to the estimation of supersaturation. It results in a very deep understanding of the µSAS process.

EXPERIMENTAL SECTION

Chemicals

Carbon dioxide was purchased from Messer. Tetrahydrofuran, inhibitor-free, ≥ 99.9 %, and 1,1,2,2-tetraphenylethylene 98% were purchased from Sigma-Aldrich and used as received.

High Pressure FTIR solubility measurements

As mentioned above, the thermodynamic properties of the {CO_2/solvent/solute} ternary system are very important in the SAS process. As a first step, the solubility of TPE was measured in various CO_2/solvent mixtures, to determine the best operating conditions. To do so, FTIR measurements were carried out under pressure, using a high-pressure optical cell (HPOC) previously described [18] (Figure 1). The HPOC (internal volume 2.2 mL) was equipped with silicon windows with a path-length of 600 µm. IR beam passed through silicon windows in the top part of HPOC. Four heating cartridges were used to control the cell temperature, while a stirrer bar placed in the bottom of the HPOC ensured a homogenous mix. FTIR measurements were performed through the two silicon windows using a ThermoFisher 6700 FTIR spectrometer (resolution: 4 cm^{-1}, spectral range: 500-6000 cm^{-1}) and analysed with the OMNIC software.

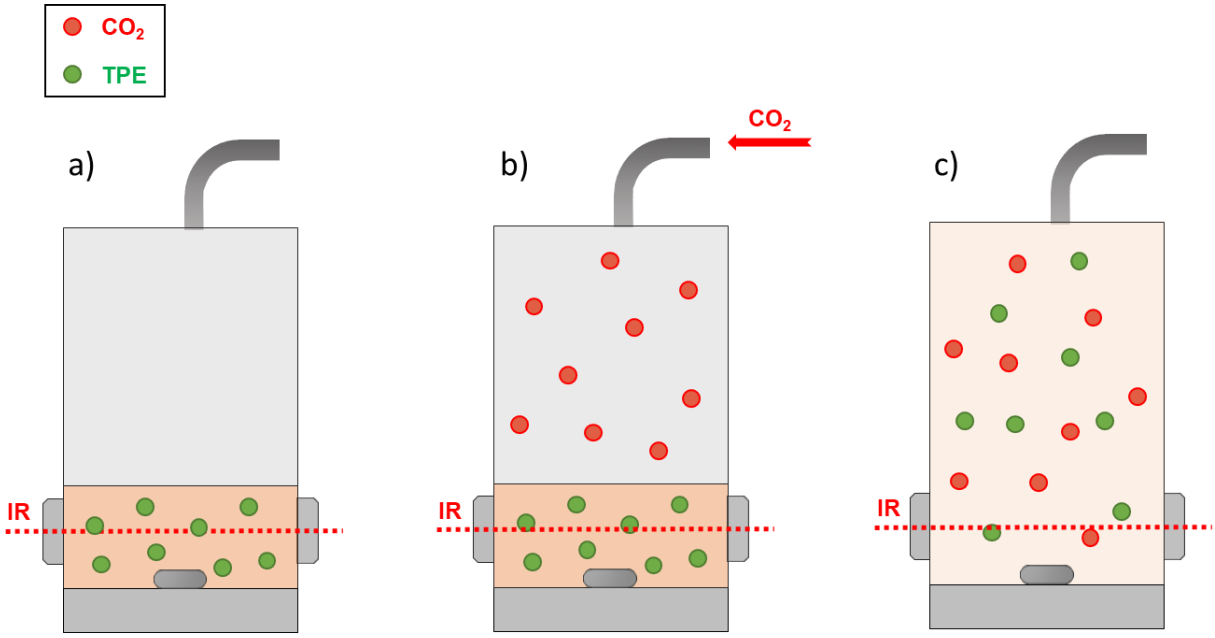

Figure 1: Schema of the high-pressure optical cell (HPOC). (a) Study of saturated solution of TPE in THF. (b) Pressurization of the cell by CO_2 injection. (c) *in situ* IR measurement of TPE solubility at 40 °C and 100 bar.

In a typical measurement, the HPOC was filled under vacuum with a very concentrated solution of TPE in THF (20 mg of TPE dissolved in 2 mL of THF). The injected solution volume ranged from 0.5 mL to 2.2 mL (total cell volume), depending on the solvent/antisolvent ratio. The cell was then heated up to 40°C, which was selected as the operating temperature for the final µSAS experiment, based on the thermodynamic phase behavior of the THF/CO_2 system (See Fig. SI-1). Then, CO_2 (liquefied from the tank through a cryostat set-up at 6°C) was added into the HPOC using a manual pump (Top Industrie) and the pressure was slowly increased up to 100 bar, a value selected for the same thermodynamic reason as for temperature (see Fig. SI-1). The cell was closed and kept under stirring during the measurements. The FTIR spectrum displayed several absorption bands, characteristic from each component of the ternary mixture (figure 2). Specific bands were selected for each of them. The CO_2 absorption bands at 4950 cm^{-1} corresponds to the combination mode $\nu_1+2\nu_2+\nu_3$ of the bending mode (ν_2), the symmetric (ν_1) and antisymmetric (ν_3) stretching of CO_2, the THF absorption band located at 1970 cm^{-1} is related to the first overtone of the ring deformation and the TPE absorption band at 1600 cm^{-1} corresponds to the aromatic "quadrant stretching" [19]. The absorbance intensity can be directly linked to molecular concentration through the Beer-Lambert law: $A = \varepsilon \cdot L \cdot c$, where A is the sample absorbance; ε is the molar extinction coefficient ($L.mol^{-1}.cm^{-1}$); L is the optical path length (cm) and c is the sample concentration ($mol.L^{-1}$). The CO_2 molar extinction coefficient at 4950 cm^{-1} was determined in a previous work using the same set-up and the same path-length [20]. The THF concentration in the ternary mixture under pressure was indexed on the pure THF concentration and on its absorption at 1 bar, assuming no variation of the molar extinction coefficient with pressure [21]. As the molar extinction coefficient of TPE at 1600 cm^{-1} was unknown, a weighted amount of TPE was dissolved in pure THF at 40 °C and 1

bar, and the measurement of the absorbance allowed us to deduce the molar extinction coefficient according to the Beer-Lambert law. As previously shown by Ollagnier et al. [22], an inhomogenous mixture leads to a shift of the baseline of the IR spectra toward higher absorbance resulting from an increased scattering of the infrared light. This phenomenon was not observed in our experiments, indicating a homogeneous ternary mixture. Furthermore, the equilibrium was considered to be achieved when no changes in the intensity of the spectral bands were noticed.

Experimental set-up and protocol

Microreactor. The homemade high-pressure microfluidic reactor [23] developed for this study was built out of silicon (chemically-etched after a photolithography step through a mask, resulting in trapezoidal crossed section channel) and Pyrex for withstanding the high pressure conditions needed for the µSAS process. The design was similar to the one published in a previous study (Figure 2) [24]. In a nutshell, it consists in a preheating side channel (width = 200 µm, depth = 130 µm) for CO_2 that reaches a main channel (width = 430 µm, depth = 230 µm) in which a silica capillary (I.D. = 100 µm, O.D. = 164 µm) is inserted and further epoxy-glued. This design creates a full 3-D coaxial injection of the solute solution (through the silica capillary) within a CO_2 outer flow (from the side channel). A compression part allows connecting the microchip to the external equipment. A heating tape equipped with an internal thermocouple, placed on the silicon back side of the microreactor, allows the temperature inside the microchannel to be controlled.

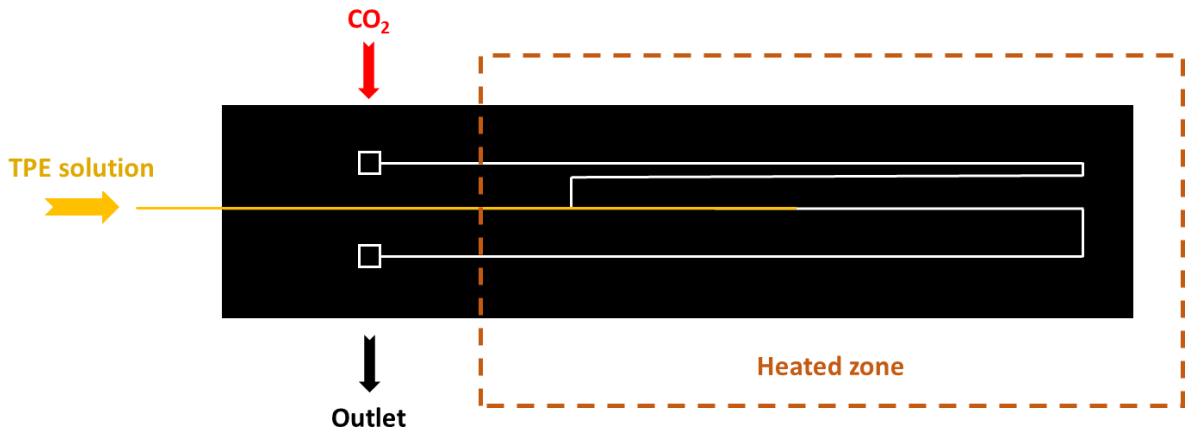

Figure 2: Schema of a Silicon-Pyrex microchip.

Set-up. The microreactor was implemented within a general set-up, presented in Figure 3. The outlet of the microreactor was connected to a recovery cell made from a sapphire tube (I.D.: 7.3 mm, O.D.: ½", length = 10 cm) able to withstand pressure up to 200 bar. The sapphire cell was equipped with a polyvinylidene fluoride (PVDF) filter (Durapore membrane filter, hydrophilic PVDF, 0.1 µm pore size, purchased from Sigma-Aldrich) placed on a metallic frit (1 µm pore size). A TEM grid Cu 300 mesh purchased from Sigma-Aldrich was laid on the filter for direct analysis of the produced particles at the

end of the µSAS process, without any particular sample preparation step. The whole recovery cell was plunged in a water bath heated at 40 °C.

The initial solution [THF + TPE] was placed inside a vial, stirred (200 rpm) and heated at 40 °C with a magnetic hot plate. It was directly injected into the microreactor using a PU-4180 continuous Jasco pump. Two other cooled Jasco pumps were used for delivering CO_2 inside the microreactor (PU-4380) and into the recovery cell for the drying step (PU-4387), respectively. The pressure in the whole system was controlled with a Jasco automatic Back Pressure Regulator (BPR) (BP-4380) placed at the outlet of the set-up (100 ± 1 bar), in which the temperature is fixed at 40°C to avoid any dry ice formation during depressurization, which could plug the system.

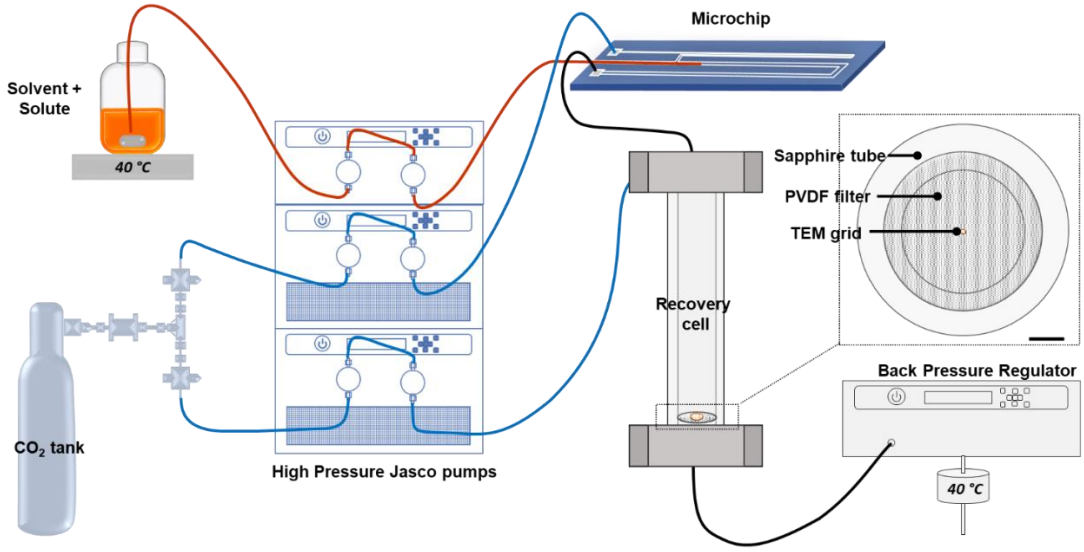

Figure 3: Scheme of the µSAS set-up.

Experimental protocol. In a typical experimental µSAS process, the temperature of the initial [THF + TPE] solution, microchip, recovery cell and BPR was set at 40°C. Then, the entire system was pressurized with CO_2 up to 100 bar. The injection of CO_2 was kept continuous at a fixed flow rate and the pressure was stabilized. Then, the [THF + TPE] solution was injected into the microreactor at a constant flow rate, leading to the creation of a co-flow mixing inside the main microchannel of the microfluidic device. The flow rates of CO_2 and [THF + TPE] solution were kept constant during a single experiment. At the end of the experiment, the solution pump was stopped and CO_2 was injected inside the recovery cell in order to perform the drying step aimed at removing any residues of THF from the synthesized powders. The programmable BPR reduced the pressure from 100 bar to atmospheric pressure within the course of 30 min (3.33 $bar.min^{-1}$).

Transmission electron microscopy (TEM)

The TEM grids placed inside the recovery cell were collected, dried, and directly analyzed with a JEOL JEM-1400+ transmission electron microscope for the characterization of organic NPs. A working

tension of 60 kV was chosen to avoid any issue with the potential deterioration or melting of the organic NPs during characterization. The Cu Mesh300 grids were purchased from Sigma Aldrich and the obtained TEM images were processed with ImageJ software for size measurements. Careful attention was brought to the measurement of the particle size, because the determination of surface tension requires to compare simulation results with very precise experimental particle size distribution. Therefore, only well-defined particles (with a clear and complete round shape, see orange circles in Figure 4b) were considered. Thanks to the large number of recovered particles (see Figure 4a), it was possible to use several images from the same TEM grid with the same magnification (×50000) to count more than 100 particles per experiment.

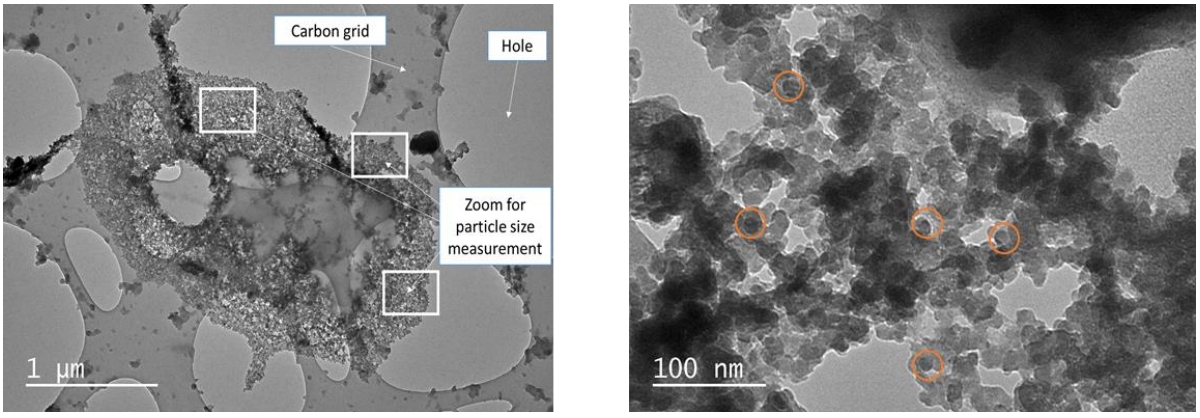

Figure 4: Cu mesh grid (a) and representative TEM images (b) for manual counting

NUMERICAL SECTION

Modelling

The numerical approach allows taking into account all the physical phenomena involved in the process. The method consists in the coupling between a computational fluid dynamics (CFD) code, to consider the thermo-hydrodynamic effects, and a population balance equation (PBE) to take into account the nucleation and growth of particles [24–26]. All the equations, established in previous studies by our group, are presented in the appendix. It was chosen here to point out only the main aspects of the model. The hydrodynamics equations (continuity and Navier Stokes equations [16]) are solved for a completely miscible fluid. Furthermore, the isothermal fluid is far from the mixture critical point, so the isothermal compressibility is relatively low (between 10^{-8} and 10^{-9} Pa^{-1}). In this case, even if the density depends on the composition of the mixture, the thermo-compressible effects are negligible. The comparison of simulations between an incompressible and a compressible formulation [27] has shown that the results were not significantly different. Because CPU time is much lower, the incompressible formulation is

chosen. The gravity is neglected in the confined microchip because of the small value of the Bond number. The Reynolds number of the simulation varies from 3000 to 12000. One of the originality of the simulation is to perform Direct Numerical Simulation down to the Kolmogorov scale, in this way we do not need any turbulence model. The evolution of each species is calculated by the resolution of the classical species conservation equations by considering advection and ideal diffusion [16]. The density is estimated by the Peng Robinson EOS, coupled with the Van der Waals mixing rule. A binary interaction parameter kij equal to -0.0027 is considered [28].The diffusion coefficients are calculated by the Hayduck and Minhas correlation [16]. The mixture viscosity is computed by classical logarithmic mixing rules. The viscosities of the pure fluids, CO_2 and THF, are obtained from the NIST database for the considered experimental conditions.

The formation of the solid particles is taken into account by a population balance equation. As the precipitated particles obtained experimentally in the microreactor are very small, we assume that the effect of the breakage and the agglomeration can be neglected. In order to solve numerically the population balance equation, we introduce the standard method of moments (SMOM). Based on its definition, the four first moments (j = 0, 1, 2, 3) have physical meanings and are solved in the simulation (m_0 is the total particle number; m_1 the total particle length; m_2 the total particle surface area; m_3 the total particle volume).

The supersaturation *S*, driving force of the precipitation, is simply defined as the ratio between the concentration of species *C* [29], deduced by the resolution of the hydrodynamic equations, and the solubility of TPE (C_{sat}) that was experimentally determined:

$$S = \frac{C}{C_{sat}} \tag{1}$$

In this work, we have considered that the primary homogeneous nucleation B is the main mechanism of the nuclei formation and it is expressed by [24]:

$$B = 1.5 D_{wc} \left(C_{sat} S N_a\right)^{7/3} \sqrt{\frac{\sigma}{k_b T}} V_m \, exp\left(- \frac{16\pi}{3} \left[\frac{\sigma}{k_b T} \right]^3 \frac{V_m^2}{ln^2(S)} \right) \tag{2}$$

with N_a the Avogadro constant, σ the solid-fluid interfacial tension, k_b the Boltzmann constant and V_m the solute molecular volume, D_{WC} the solute diffusion coefficient calculated by the correlation proposed by Wilke and Chang [30]. As the solid-fluid interfacial tension σ in Equation 2 is unknown, its value is fitted with the experimental results. The growth rate is calculated as a function of the supersaturation and a mass transfer coefficient k_g deduced from the Sherwood number which is estimated thanks to the Froessling correlation.

Numerical methods

The system of the partial derivatives equations (detailed in appendix) is numerically solved by the homemade Fortran CFD code "Notus" (https://notus-cfd.org/), developed at the Institute of Mechanical Engineering (I2M-TREFLE). Notus is an open source software based on the finite volume method. The variable fields are solved on a fixed staggered grid. Since Notus is massively parallel, it allows simulating 3D configuration with great precision. The formulation employed is totally explicit, except the pressure correction step in the velocity-pressure coupling algorithm which is solved implicitly. The Navier-Stokes equation is solved in two steps by the time-splitting algorithm of Goda [31]. The advection term is discretized by the second order scheme in space (total variation diminishing with superbee flux limiter function (TVD superbee)) [32] and an explicit second order central discretization is applied in space for the diffusion term. The trapezoidal shape (figure 5) of the domain is taken into account by an immersed boundary method [33]. At the inflow boundary, a flat constant profile is imposed in the coflow and a laminar Poiseuille flow profile for the injector. A zero-gradient boundary condition is applied to the outlet boundary, and no-slip boundary conditions for the remaining boundary conditions.

Due to the trapezoidal asymmetrical geometry (Figure 5), a three-dimensional simulation is required. As demonstrated in our previous study [16], the Kolmogorov and Batchelor scales in our system are in the micrometer range. So we chose an uniform mesh, the grid size of which is $\Delta x = \Delta y = \Delta z = 3\mu m$ for a total number of nodes of 14.5 millions for a channel length of 4 mm. This is a good compromise between precision and CPU time.

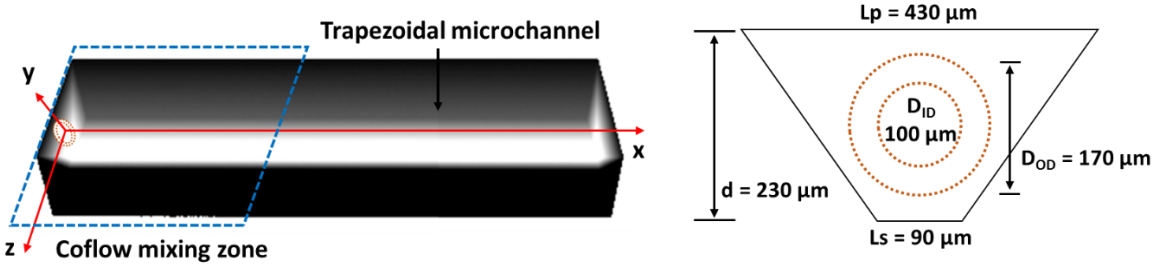

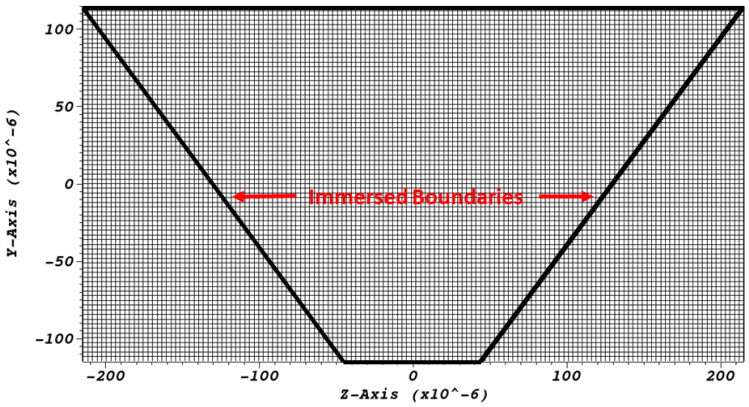

Figure 5: The geometry of the numerical microchannel for the turbulent mixing simulations showing the three dimensional trapezoidal microchannel, the dimension of the cross-section at x = 0 and the mesh in the yz plane and location of immersed boundaries.

RESULTS AND DISCUSSION

TPE solubility in the [CO_2 + THF] mixture at 40°C and 100 bar

The solubility of the TPE in the [THF + CO_2] mixture was determined for different solvent/antisolvent ratio at fixed conditions of pressure and temperature, selected for the final µSAS process (100 bar and 40 °C). The FTIR spectra, for different molar ratio, are obtained (Figure 6) in order to determine the species concentration at equilibrium.

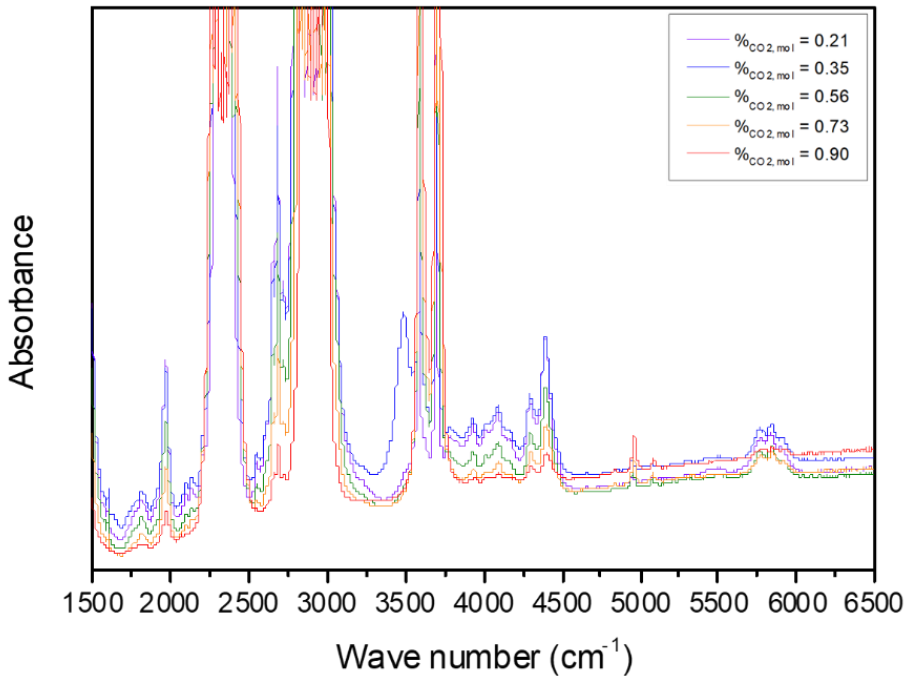

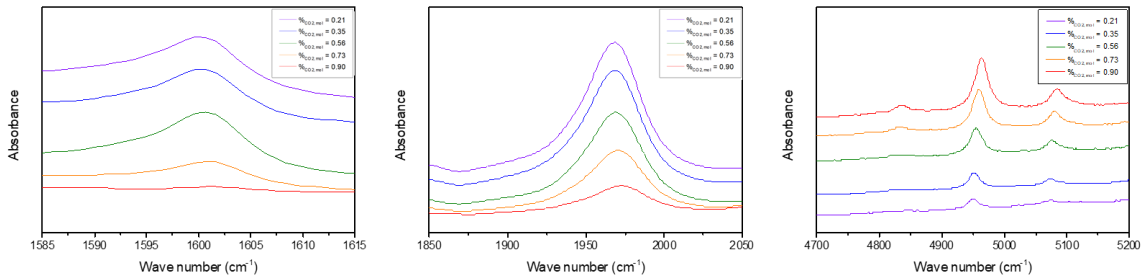

Figure 6: Selected regions of the FTIR spectra of {CO_2/THF/TPE} system from different CO_2 molar ratios at T = 40°C and p = 100 bar. 1: TPE absorption band, 2: THF absorption band, 3: CO_2 absorption band.

The solubility values deduced from the experimental measurements are presented in Figure 7 and fitted with a simple analytical model. This one estimates the evolution of the solubility x_{sat} (mol/mol) in function of the CO_2 molar fraction x_{co2}:

$$x_{sat} = 0.0011\left(1 - x_{co2}\right)^{1.0051 - 2.5871x_{co2} + 3.4422x_{co2}^2} + 6.7.10^{-6}\, x_{co2} \qquad (3)$$

As seen, the solubility of TPE (mol TPE / (mol CO_2 + mol THF)) decreased continuously with increasing the proportion of CO_2 into the binary solvent system [THF + CO_2] mixture, ranging from 1.1×10^{-3} mol/mol in pure THF to 6.7×10^{-6} mol/mol in pure CO_2. Interestingly, no noticeable co-solvent effect was detected, showing that CO_2 actually acts as an anti-solvent for all the considered compositions. To generate high supersaturation and access good mixing conditions in the µSAS process, it was chosen to work with a CO_2 molar fraction of 98%, at 40 °C and under an operating pressure of 100 bar.

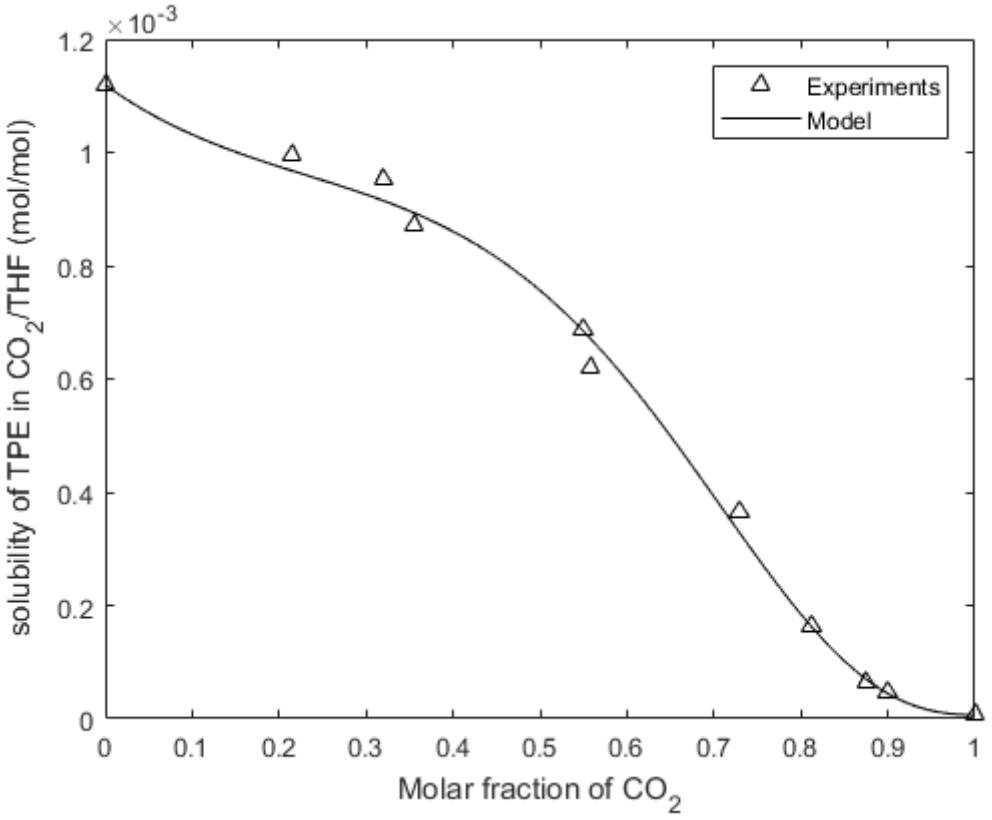

Figure 7: TPE solubility in the binary {THF + CO_2} system at 40 °C and 100 bar as a function of the molar fraction of CO_2 in the mixture.

Processing of TPE NPs with the µSAS process

Nanoparticles of TPE were then prepared using the µSAS device. Some experimental parameters were allowed to vary, in order to observe their impact on the shape, size and size distribution of the synthesized NPs. More precisely, three µSAS experiments were conducted by changing the initial TPE concentration in the THF solution (2 $g.L^{-1}$ and 3 $g.L^{-1}$), as well as the CO_2 and solution flow rates (passing from 8 and 0.4 mg/min, respectively, to 2 and 0.1 mg/min), for the same solvent/antisolvent ratio. For the latter parameter, the objective was to compare the effect of the mixing regime, determined by the mean Reynolds number – *Re* [16] (laminar – *Re* = 3000 or turbulent – *Re* = 12000), on the NP size. Indeed, high Reynolds number flow allows reaching very fast mixing, as previously reported in a former study [16]. The shape and size of the NPs were observed by TEM. Typical TEM pictures are shown in Figure 8, displaying small NPs slightly agglomerated on the grids. All NPs exhibited spherical shapes, with a very small mean diameter ranging from 9 to 14 nm. The size dispersion was calculated (Figure 9). All experiments have been repeated three times to validate the reproducibility of the process. Table 1 summarizes all the considered conditions along with the TPE NPs characteristics.

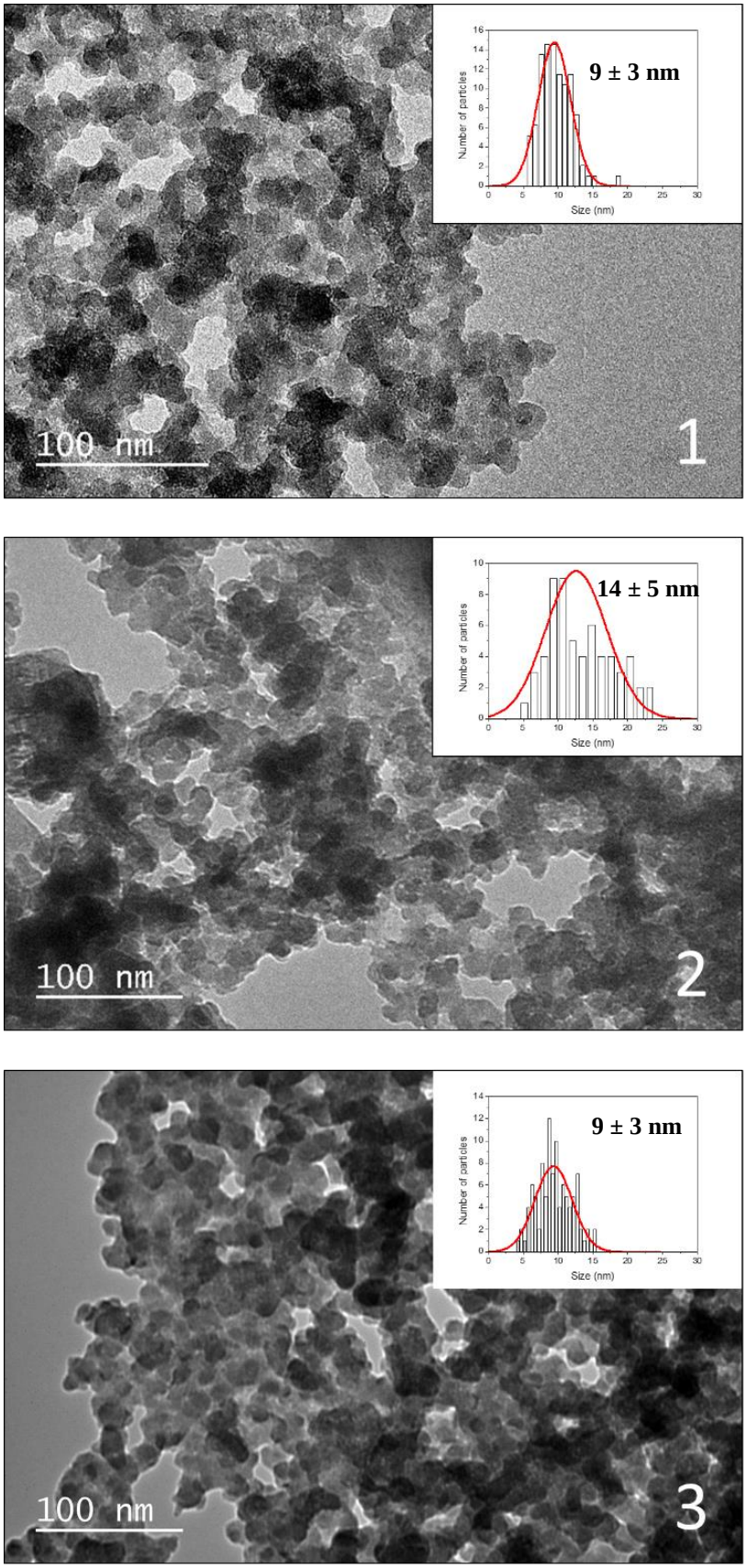

Figure 8: TEM images of TPE NPs synthesized by µSAS at 40 °C and 100 bar. Experiment number is integrated on the image. Inset: corresponding size distribution.

Table 1: Process parameters (initial TPE concentration $[TPE]_i$, mass flow rates Q_m) for TPE synthesis by µSAS (T = 40°C, P = 100 bar), Reynolds numbers *Re*, and mean size of the NPs measured from TEM images.

Exp. No.	$[TPE]_i$ in THF	Q_m CO2 $mg.min^{-1}$	Q_m THF $mg.min^{-1}$	*Re*	Mean size (nm)
1	2 $g.L^{-1}$	8	0.4	12000	9 ± 3 nm
2	2 $g.L^{-1}$	2	0.1	3000	14 ± 5 nm
3	3 $g.L^{-1}$	8	0.4	12000	9 ± 3 nm

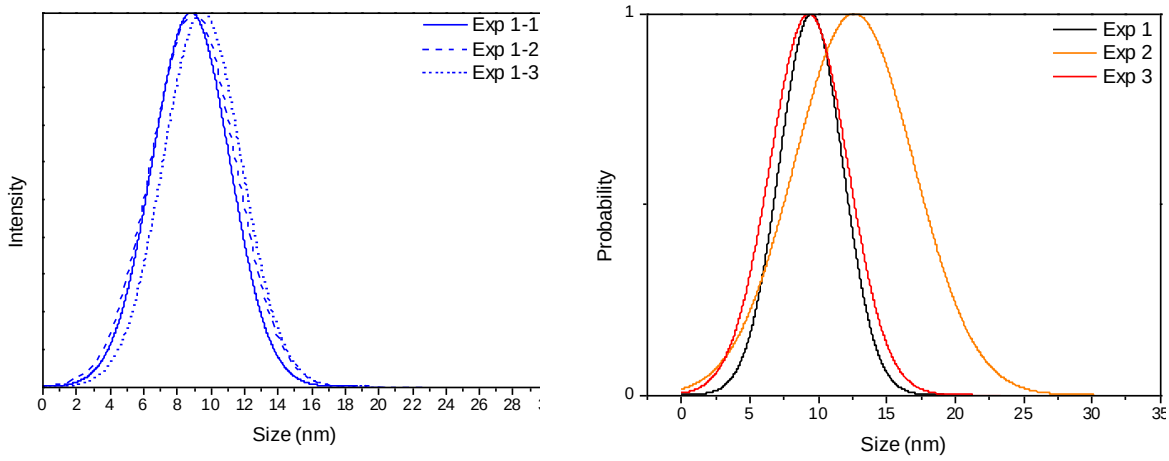

Figure 9: a) Size distributions of TPE NPs obtained from experiment No.1 repeated three times (Reproducibility); b) Normalized size distributions of the TPE NPs prepared under the three experimental conditions.

The comparison of samples **1** and **3** showed that the initial concentration of TPE, in the studied range, had no effect on the particle size, and only a slight effect on size distribution. In contrast, the effect of the mixing regime is obvious when comparing samples **1** and **2**. The NPs were significantly smaller in sample **1** (9 nm ± 3 nm) than in sample **2** (14 ± 5 nm), and their size distribution was much narrower. This behavior was expected because very fast mixing is achieved at high Reynolds number flows (in particular in turbulent conditions), leading to a high burst of nucleation in a very short period of time, and leaving almost no dissolved TPE for the growth. This results in small NPs, and narrow particle size distribution. Oppositely, in the case of sample **2**, the flow rates are reduced four times, and so the mixing time is increased, as numerically demonstrated in the next section. Hence, due to less favorable mixing, the nucleation rate is lower, so growth is promoted consequently leading to bigger particles.

µSAS simulation results

The simulations were carried only out for the experimental conditions 1 and 2 reported in Table 1 in order to demonstrate the influence of the mixing conditions for NPs synthesis. Concerning the influence of the concentration, no significant influence has been observed experimentally. This is due to the very low solubility of the TPE in the THF. As discussed in the introduction, all parameters of the numerical simulation can be estimated except the interfacial tension σ between the solid and the fluid phase. Because of the lack of knowledge of this crucial parameter, its value was estimated by fitting the simulation results to the experimental data.

Determination of the interfacial tension σ

The particle size distribution was calculated by applying a log-normal distribution according to the time average values of the moments [25]. The interfacial tension σ was estimated to be 2.25 mN/m for experiment No.1. This value resulted in the best agreement with the particle size and size distribution obtained from the µSAS experiment. The comparison between the numerical particle size distributions and the experimental one is represented in Figure 10. We can observe a very strong influence of the surface tension σ on the distribution. Indeed, a variation between 2 and 3 mN/m can lead to very different size distributions and width.

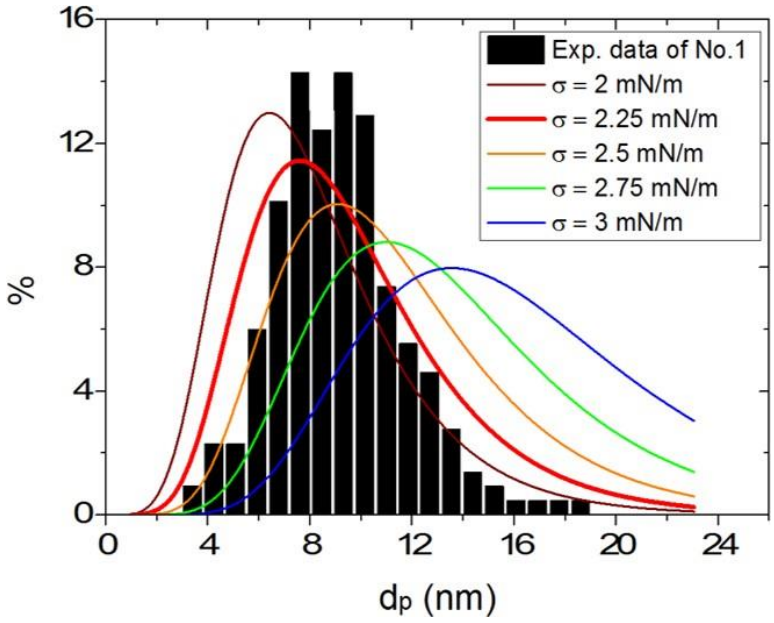

Figure 10: Bar chart: Size and size distribution of TPE particles prepared experimentally using the µSAS process according to the reference test case No.1 (Table 1). Colored curves: simulated particle distributions as a function of the interfacial tension σ.

General analysis of the reference case (No.1)

Several fields of important variables were illustrated and analyzed for the case No.1 (Table 1). The effects of the operating parameters are presented after this general analysis.

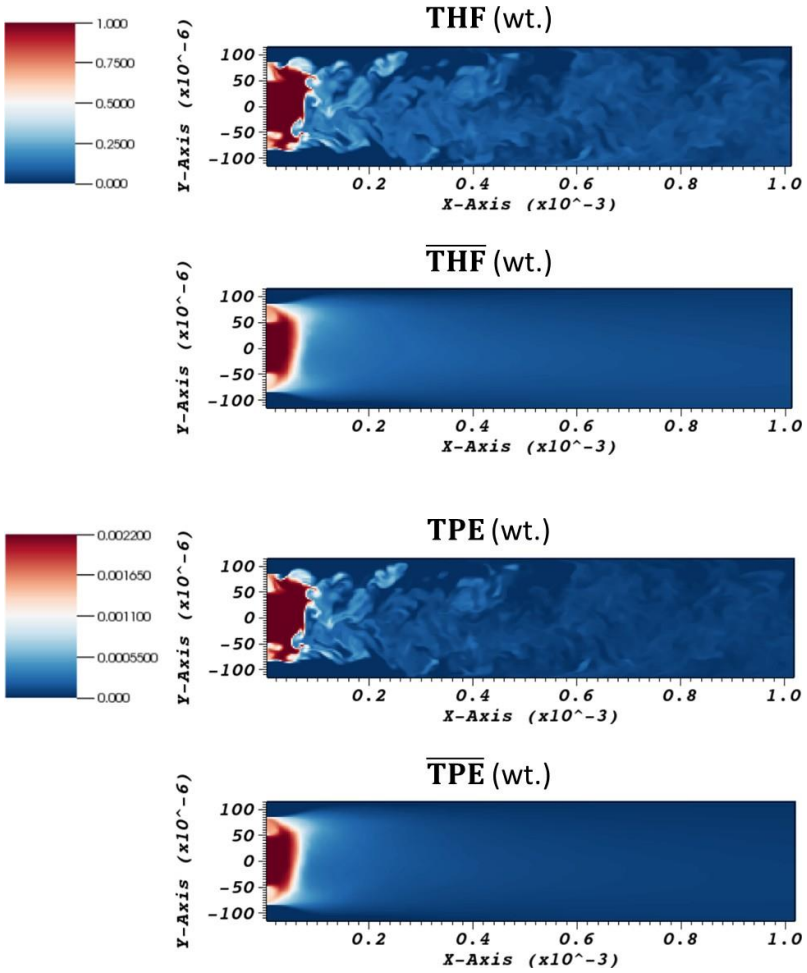

Figure 11: The instantaneous and mean time fields of the solvent THF and the dissolved solute TPE mass fractions in the microchannel of the plane z = 0 (with the unit of meter for x and y axis) for the reference case No.1.

In order to illustrate the general mixing quality of the µSAS process, we examined first the instantaneous and time averaged fields of mass fractions of THF and TPE in the plane of z = 0 in Figure 11 (which represents the depth of the channel). The species transport is very fast for both solute and solvent in the conditions of the reference test case No.1 and a homogeneous mixture is obtained within 1 mm from the capillary outlet, according to the time averaged fields. We observed that the solute TPE dissolved in the fluid mixture is consumed by the particle formation. Although the diffusivities of TPE

and THF in CO_2 are different, a similar behavior is observed between the solute TPE and the solvent THF mass fractions, resulting from much stronger effects of convection compared to the diffusion for the operating conditions.

After the first observation on the mixing quality by the mass fraction distributions, we analyzed quantitatively the fluid mixing by providing the instantaneous and mean time fields of the engulfment micromixing time [34] $t_{mE} = 17.24\sqrt{\frac{\upsilon}{\varepsilon}}$ in the plane z = 0 (Figure 12). The dissipation rate of the turbulent kinetic energy ε was calculated by the following relation:

$$\varepsilon = 2\nu\left[\begin{array}{c}\left(\frac{\partial u_x'}{\partial x}\right)^2+\left(\frac{\partial v_y'}{\partial x}\right)^2+\left(\frac{\partial w_z'}{\partial x}\right)^2+\left(\frac{\partial u_x'}{\partial y}\right)^2+2\left(\frac{\partial v_y'}{\partial y}\right)^2+\left(\frac{\partial w_z'}{\partial y}\right)^2 \\ +\left(\frac{\partial u_x'}{\partial z}\right)^2+\left(\frac{\partial v_y'}{\partial z}\right)^2+2\left(\frac{\partial w_z'}{\partial z}\right)^2+2\left(\frac{\partial u_x'}{\partial y}\frac{\partial v_y'}{\partial x}\right)+2\left(\frac{\partial u_x'}{\partial z}\frac{\partial w_z'}{\partial x}\right)+2\left(\frac{\partial w_z'}{\partial y}\frac{\partial v_y'}{\partial z}\right)\end{array}\right] \quad (4)$$

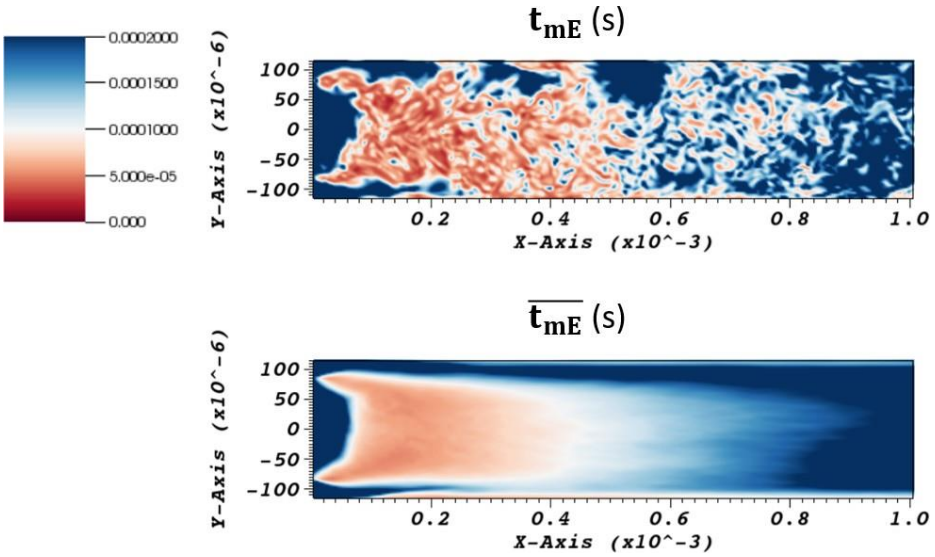

Figure 12: Engulfment micromixing time in the microchannel of the plane z = 0 (with the unit of meter for x and y axes) for the reference test No.1.

The engulfment micromixing time t_{mE} is in the order of magnitude of 10^{-5} s (0.01 ms) for the examined conditions, illustrating that the mixing rate is extremely high, especially at the beginning of the mixing close to the capillary outlet. This result is related to the high velocity fluctuations of fluid mixture in this zone, creating high turbulent energy dissipation rate up to 10000 $W.kg^{-1}$ locally in certain cells (Figure 13). According to the mean field of the engulfment micromixing time t_{mE}, its value drops to 0 at a distance of 1 mm from the injector tip. This means that the mixing is completed due to no more energy dissipation, and the fluid mixture becomes homogeneous, corresponding well to the mass fraction field of the THF solvent in Figure 11.

In order to quantify the mixing efficiency with a single representative value, the characteristic mixing time was determined by the method presented in our previous study [16,35]. The characteristic mixing time is considered as the time constant of a function representing the global evolution of the mixing in the reactor which can be easily modeled by a first order dynamic model $f \propto e^{-\frac{t-t_r}{\tau}}$ with τ and t_r being respectively the time constant and the time delay. The global evolution of the well-known segregation intensity [36] is used to characterize the mixing. If the segregation intensity is equal to 1, the segregation between species is total, whereas a value of 1 indicates a perfect mixing. The segregation intensity I_m is calculated for each abscissa x and is defined by:

$$I_m = \frac{\sum_{1}^{N} (\omega_a - \overline{\omega}_a)^2}{N(\overline{\omega}_a(1-\overline{\omega}_a))} \tag{5}$$

with ω_a the mass fraction of the solvent THF and $\overline{\omega}_a$ the mean mass fraction of THF calculated in the plane yz for each abscissa x.

A characteristic mixing time of 0.029 ms was obtained. This very low value emphasized the excellent mixing efficiency in our microreactor under the µSAS conditions.

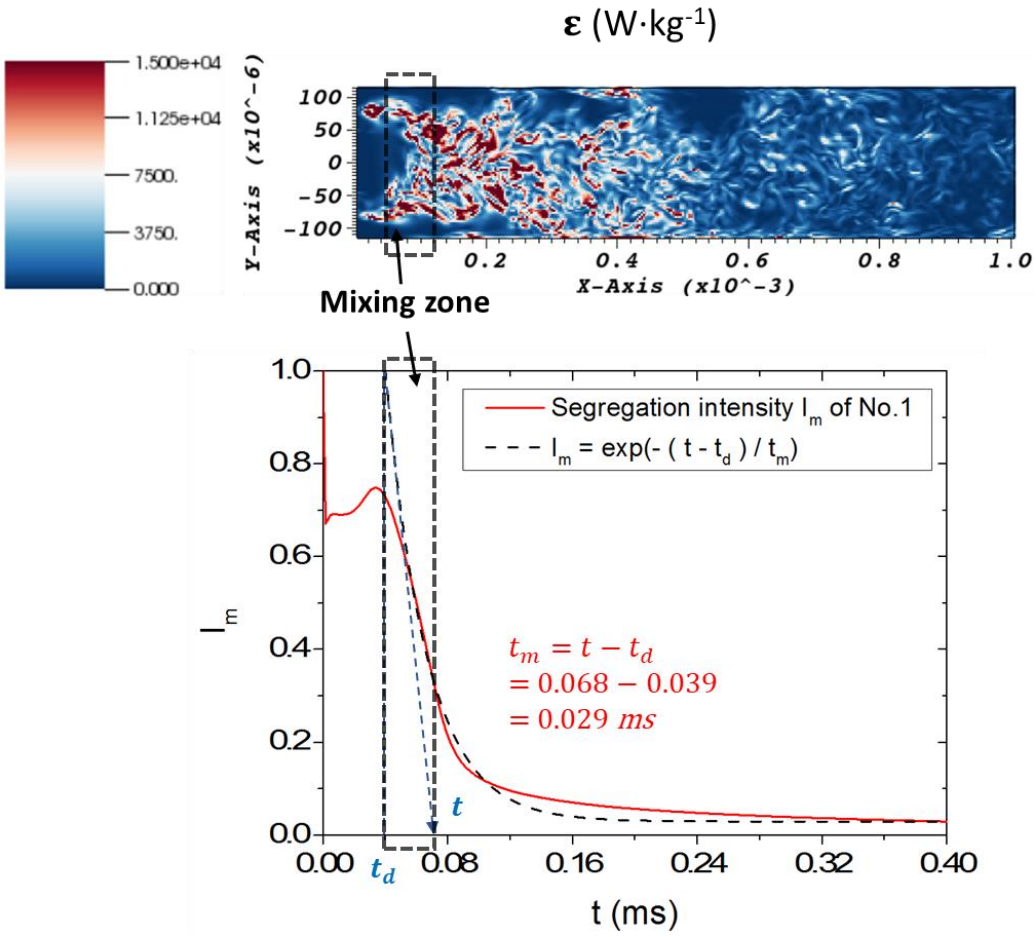

Figure 13: Instantaneous field of the energy dissipation rate ϵ of the plane z = 0 (with the unit of meter for x and y axis) and the characteristic mixing time t_m determined by the segregation intensity Im for the reference test No.1.

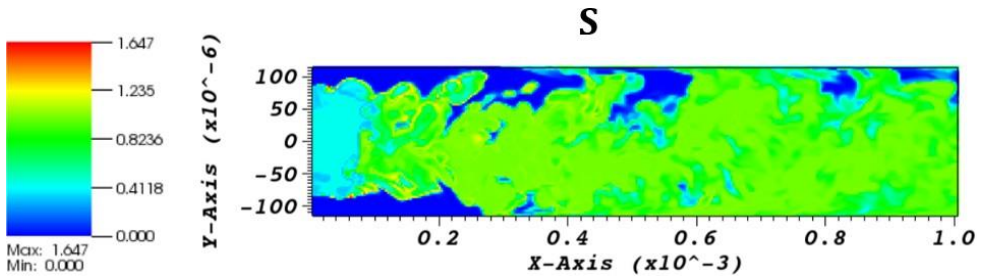

Figure 14: Instantaneous fields of supersaturation S in the plane z = 0 of test case No.1.

The influence of the fast mixing of the test No.1 can be reflected on the instantaneous fields of the supersaturation *S*, nucleation *B* and growth rate *G*. As the driving force of the precipitation, the supersaturation $S = C/C_{sat}$ was calculated in the microchannel. The instantaneous field of supersaturation is shown in Figure 14. Thanks to the efficient mixing in this case, no effective gradient was observed in the microchannel. However, the value of supersaturation was generally low with a maximum of 1.647. The first explanation is the low TPE concentration even in the initial solution. TPE cannot be dissolved in large quantities in THF, although its solubility in THF is higher than in other common organic solvents. So, the low concentration of TPE cannot offer a high value of supersaturation. The low value of supersaturation is also linked to the nucleation rate B and the particle growth rate G. In order to clearly present the relationship between nucleation and supersaturation in Figure 15, the instantaneous field of supersaturation is reset with a superior limit at 1.3 and an inferior boundary at 1 because the precipitation occurs only while the supersaturation degree is higher than 1.

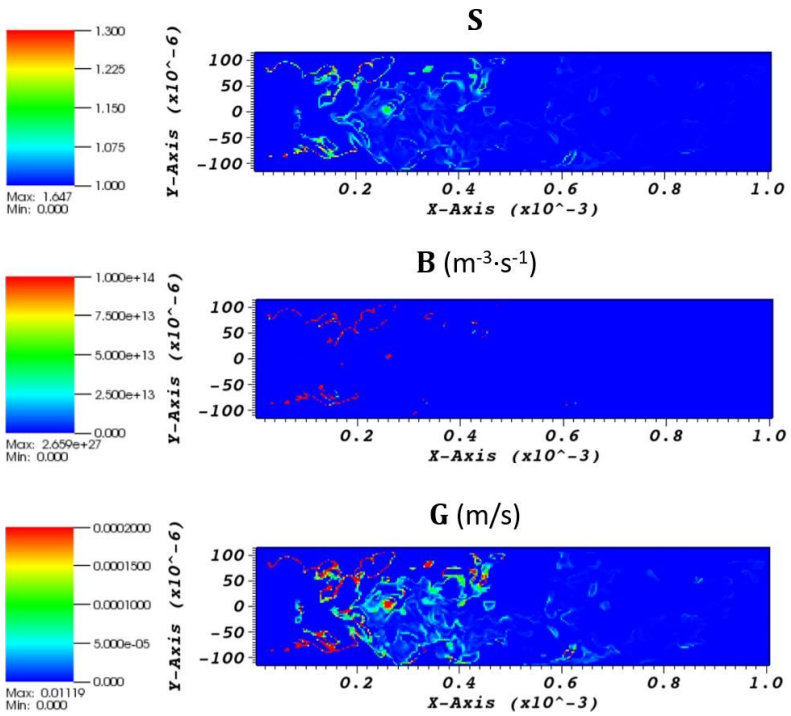

Figure 15: Instantaneous field of supersaturation S, of nucleation rate B and of particle growth G in the plane z=0 of test case No.1.

The evolution of the supersaturation can be considered as a combination of its generation by fluid mixing and its consumption by the nucleation and the particle growth (for S > 1). The extremely high rate of nucleation leads to a fast decrease of the supersaturation degree once it exceeds 1. The similarity of these two fields can be observed in Figure 15, as well as the relationship between the supersaturation and growth rate. However, the nucleation is favorable because of the fast fluid mixing. The supersaturation S drops quickly after nucleation, leaving a weak driving force for particle growth. The high nucleation rate results from the small value of the surface tension ($\sigma = 2.25$ mN/m) and a significant diffusion coeffcient for TPE particle D_{WC} (up to 1.4×10^{-8} m^2s^-1) under the supercritical mixture conditions due to a gas-like viscosity of the fluid mixture (about 43 µP.s). Indeed, these two parameters affect decisively the nucleation process and contribute to fast rates in the simulation case No.1.

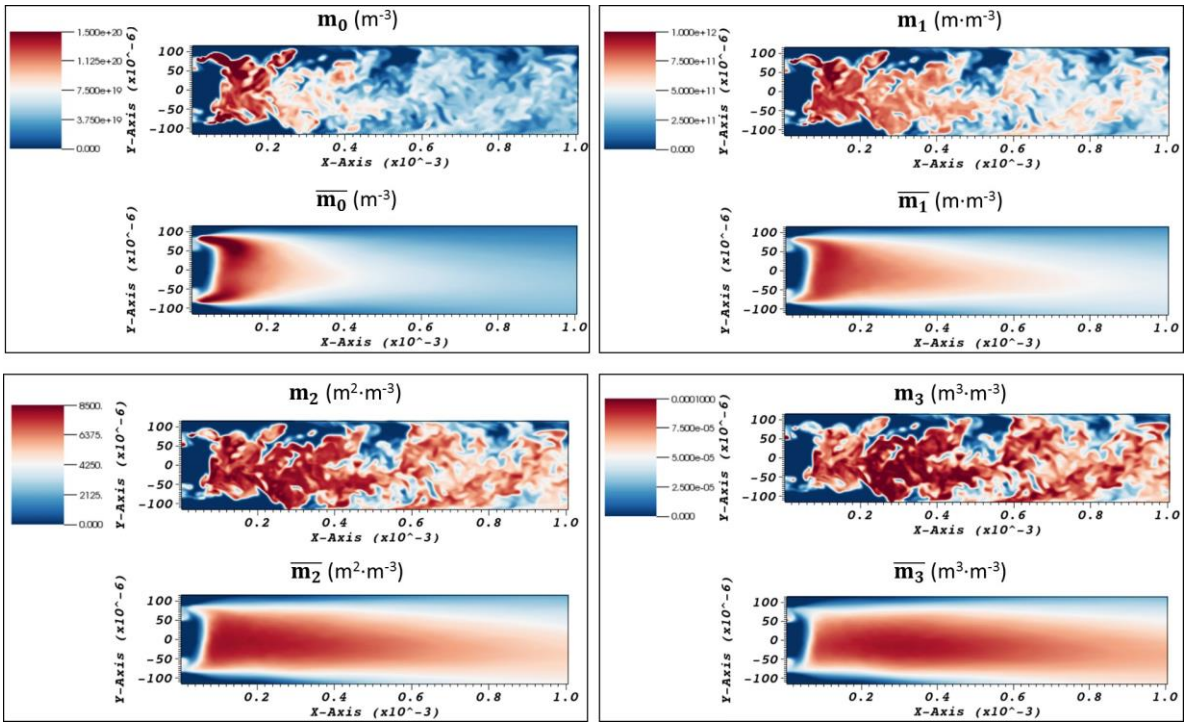

Figure 16: Instantaneous and averaged fields of the moments m_0 (total number of particles per volume), m_1 (total length of particles per volume), m_2 (total surface of particles per volume) and m_3 (total volume of particles per volume) of test No.1.

The moments m_0, m_1, m_2 and m_3 represent, per volume of the reactor, the total number of particles, the sum of the particle length, the sum of the particle surface and the total particle volume, respectively. These moments are displayed in Figure 16 with their instantaneous and time averaged fields.

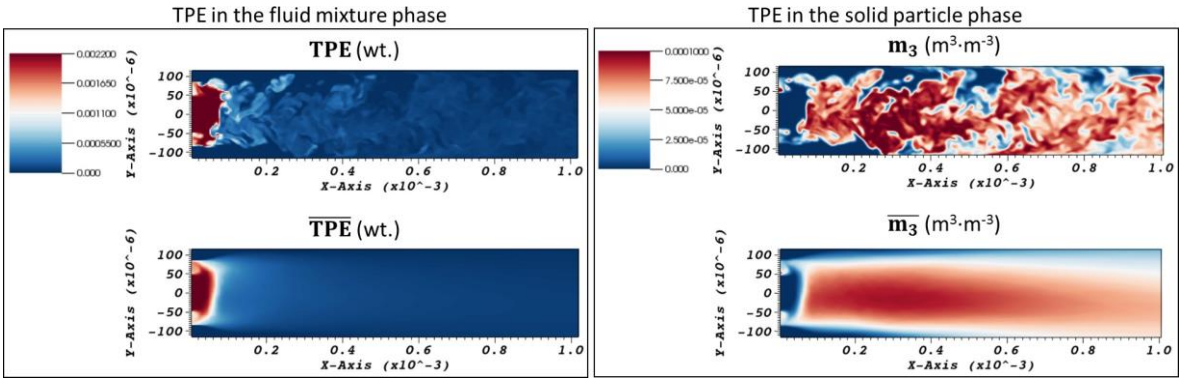

Figure 17: TPE mass fractions in the fluid phase (left) and in the solid phase (right), represented by the moment m_3 of the total volume.

As expected, the mean fields of the moments also show that the fast fluid mixing contributes to reaching homogeneity at 1 mm from the injector outlet. Figure 17 illustrates qualitatively the solute TPE in the

fluid and solid phases, which can be considered as the moment m3 for the total particle volume. This consistency proves the robustness of the numerical modeling.

The average values of the moments allow to estimate the particle size mean value. The first two moments are chosen to express the mean particle size $\overline{d_p} = \frac{\overline{m_1}}{\overline{m_0}}$. The fields of both the instantaneous and mean particle sizes can be seen in Figure 18.

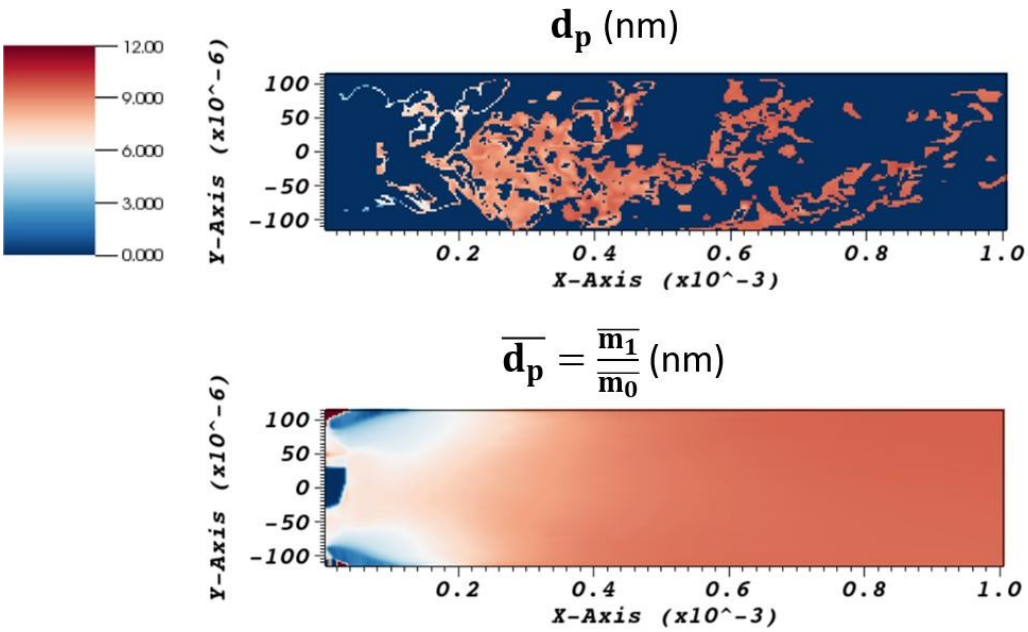

Figure 18: The instantaneous particle size field and its mean time value in the plane z = 0 of test case No.1.

By monitoring the instantaneous particle size dp, the particle growth at different locations in the microchannel was observed. The sizes varied from 6 to 15 nm, corresponding well to the experimental measurements of the test case No.1. The mean values of the particle sizes dp became stable at 1 mm from the capillary tip, which is a coherent result regarding the other time averaged fields.

Effects of the mixing conditions

After the analysis of the reference case No.1, another test case with different flowrates were investigated in order to clarify the influence of the mixing conditions. The test case No.2 for lower flow rates was simulated using the same surface tension σ=2.25 mN/m as that obtained from the reference simulation No.1. The main information are reported in Table 2.

Table 2: The TPE particle mean sizes originating from experiments (d_{pexp}) and simulations (d_{pnum}), the surface tension used in the simulations σ, the mixing times t_m at fixed temperature (40 ◦C) and pressure

(100 bar) under tested µSAS conditions (initial concentration of TPE $[TPE]_i$, mass flow rates Q_m, velocities u and Reynolds number)

No	$[TPE]_i$ g/l	Q_m CO_2 mg.min^{-1}	Q_m THF mg.min^{-1}	u_{co2} m/s	u_{THF} m/s	Re	σ mN/m	t_m ms	d_{pexp} nm	d_{pnum} nm
1	2	8	0.4	6.35	0.95	12000	2.25	0.59	9.1	9.5
2	2	2	0.1	1.59	0.23	3000	2.25	0.029	14.4	16.6

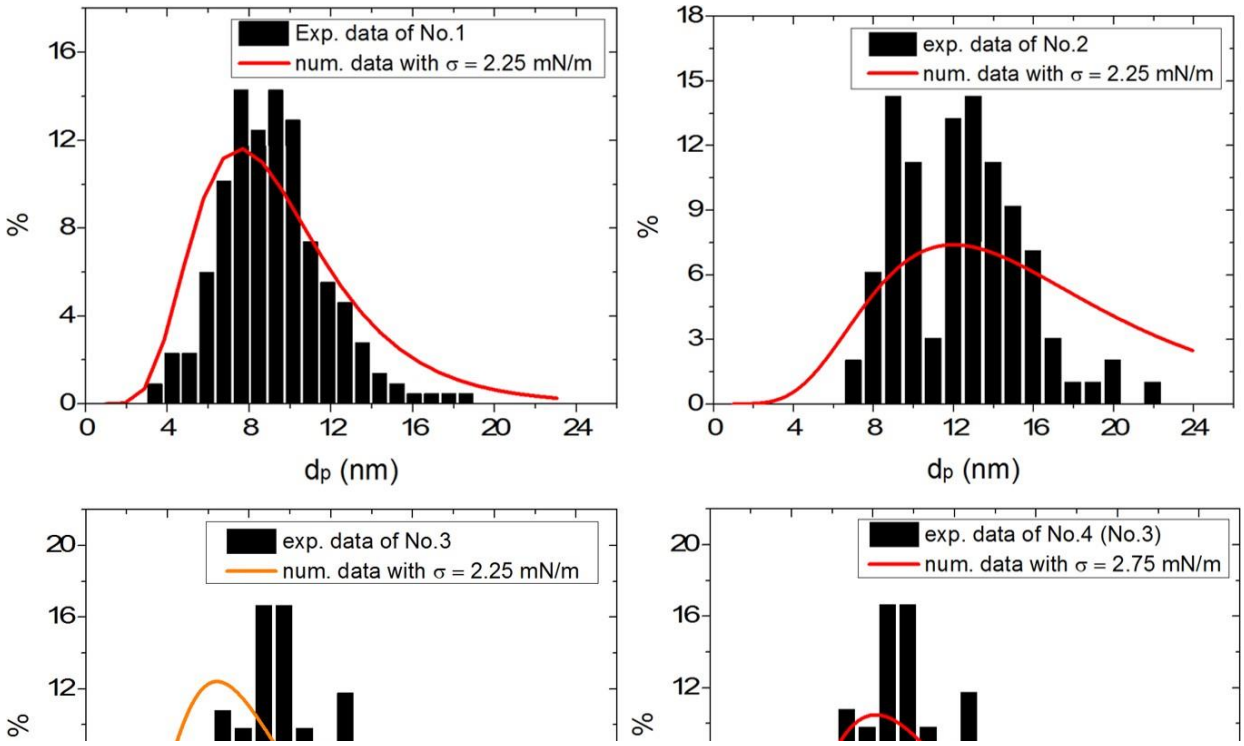

The results of the comparison between experimental and simulated distributions are shown in Figure 19. The simulations yield generally acceptable results on the particle sizes and size distributions for the two test cases.

While the flow rates of No.2 were reduced to 110 µL.min^{-1} and 2000 µL.min^{-1}, respectively, for the TPE/THF solution and the antisolvent CO_2, compared to the reference test case No.1, the mean size of TPE was increased from 9.1 nm to 14.4 nm, according to the experimental results, with the same total CO_2 mass fraction at 98%. In fact, a relative "inefficient" mixing in case No.2 can be represented by the mean time mass fractions of THF and TPE (Figure 20). A long length of solvent jet can be observed. In spite of a mixture homogeneity at x = 1 mm, the fluid is quite heterogeneous in the vicinity of the injector tip.

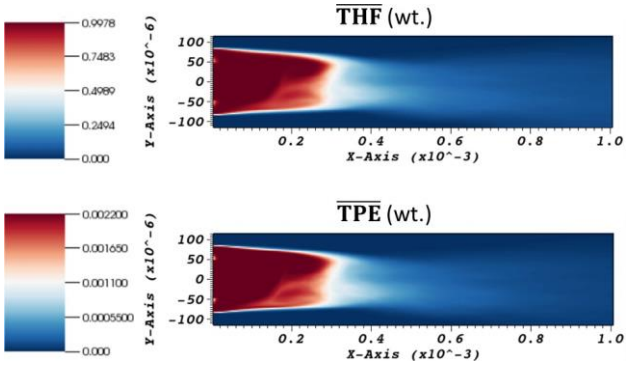

Figure 20: The mean time fields of the THF and TPE mass fractions in the test case No.2 with low flow rates.

More specifically, in order to analyze the velocity effect on the mixing time t_m, this value was deduced from the evolution of the segregation intensity (Figure 21). The decrease of fluid flow rates in test No.2 leads to slow mixing compared to the reference test No.1, with a mixing time of 0.59 ms, one order of magnitude higher than in test No.1 (0.029 ms). This less efficient mixing influences the supersaturation degree, which is slightly smaller in No.2 than in No.1, especially at the outlet of the injector. It also generates a quite heterogeneous field of the supersaturation around the long jet of the TPE/THF solution. This less uniform supersaturation field promotes particle growth instead of nucleation. In other words, in the test No.1, supersaturation is mainly consumed by nucleation close to the injector outlet once the fluids encounter each other. In contrast, in the test No.2, the length of the region where supersaturation is more than 1 is two times (1 mm) that of the reference test No.1 (0.5 mm), resulting in a longer distance and more time for the growth of the nuclei formed upstream. The slower mixing in the case No.2 can explain the increase of the mean TPE particle size.

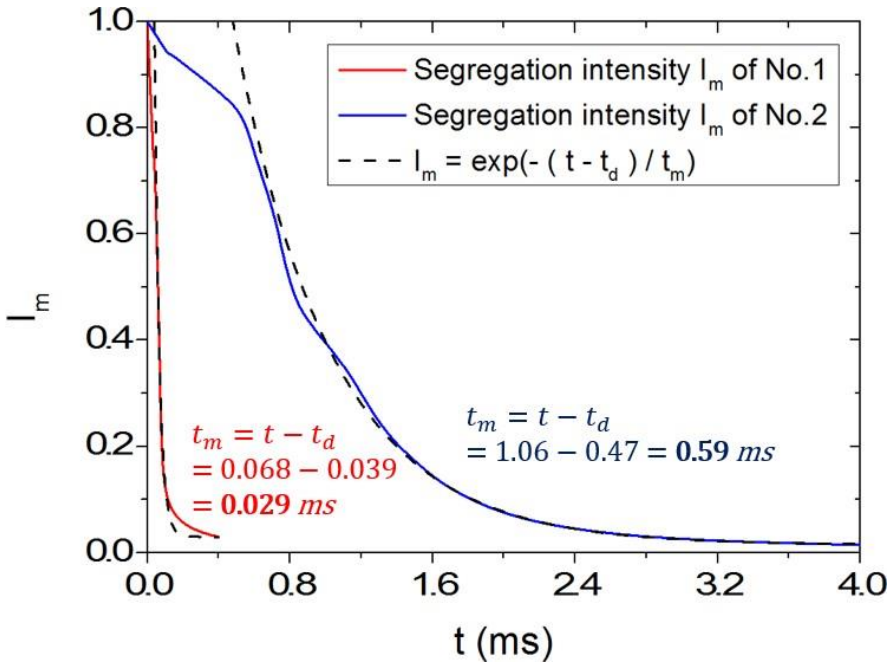

Figure 21: Intensity of segregation curves of tests No.1 and No.2 as a function of time with the determination of mixing time.

The comparison between tests No.1 and No.2 confirmed the importance of the hydrodynamic behavior of mixing in the microreactor that we emphasized in our previous study [35]. High flow rates (fluid velocities) lead to fast mixing, and so to small particle sizes and narrow size distributions.

Characteristic times of the precipitation

In order to compare the characteristic time of precipitation and fluid mixing, the time of precipitation tp has been estimated. In Figure 22, we have represented the evolution on the center line of the mean particle size dp as a function of time. The time axis t is defined as: $t = x/u_{xin}$, the same as that used for the turbulent mixing analysis in our previous study [16], with L the length of microchannel, u_{xin} the average velocity of the inner fluid TPE/THF solution, depending on its flow rate and on the inner surface of the capillary.

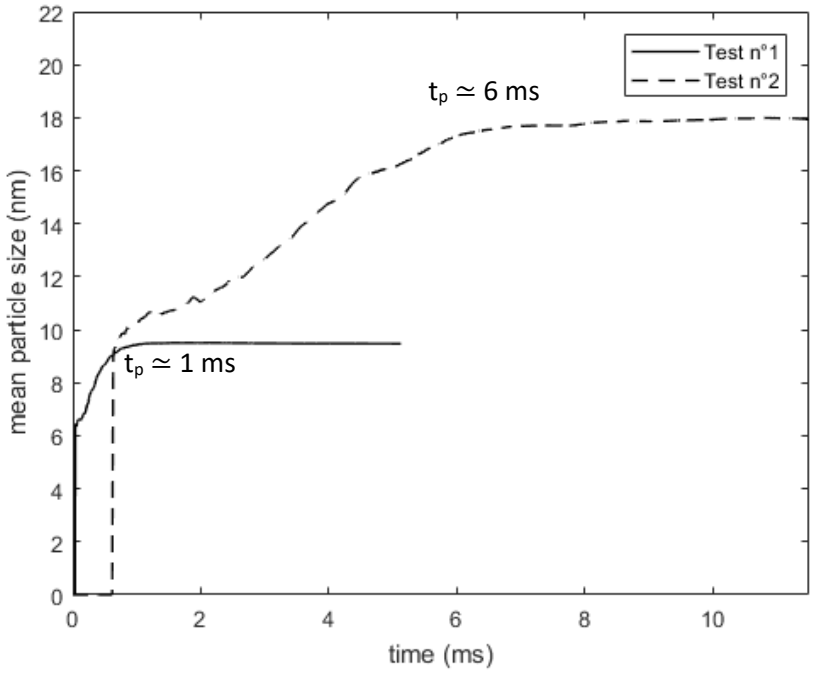

Figure 22: Determination of precipitation time t_p according to the mean particle size.

The characteristic time of precipitation t_p is defined in this study as the time when the mean particle size dp reaches a stable value (Figure 22). Another important characteristic time for the particle precipitation process is the nucleation time, which is generally not well defined. The different characteristic times are reported in Table 3 in order to compare their orders of magnitude.

Table 3: Characteristic times (precipitation time tp, estimated nucleation time tn) with the average nucleation rate B, the mean particle growth rate G and the Da numbers (Da_p for fluid mixing and precipitation, Da_n for fluid mixing and nucleation).

Test No.	t_p *(ms)*	r^* *(nm)*	$G \cdot 10^5$ $(m \cdot s^{-1})$	$B \cdot 10^{-21}$ $(m^{-3}s^{-1})$	t_n (ms)	t_m (ms)	Da_p	Da_n
1	1	1.59	5.28	2.15	0.017	0.59	0.029	1.7
2	6	2.15	3.43	1.72	0.021	0.59	0.098	28.1

The nucleation time is directly related to the average value of the nucleation rate B. It is the global mean value of space and time in the simulated microchannel, also given in Table 3 for all tested cases. We have taken the volume of the discretized cell ($V_{cell} = 3 \times 3 \times 3\ \mu m^3$) as the considered volume, and the characteristic nucleation time t_n can be estimated as:

$$t_n = \frac{1}{BV_{cell}} \tag{6}$$

This method provides nucleation times of reasonable order of magnitude of 10^{-5}s. The values of the two test cases are close due to the same range of supersaturation and constant surface tension. To compare the characteristic times of the fluid mixing and nucleation, we introduced here the dimensionless Damköhler number Da, often used to relate the reaction rate to the species transport rate:

$$Da = \frac{mixing\,time}{reaction time} \tag{7}$$

The Da number was calculated for both TPE precipitation (Da_p) and nucleation (Da_n), with t_m, t_p and t_n in Table 3. We confirm and emphasize that our microreactor can provide a high efficient fluid mixing under µSAS conditions with a very low Da number of precipitation Da_p, even for a relatively slow mixing (test No.2), indicating that the fluid mixing is much faster than the entire precipitation process. The mixture becomes homogeneous much before the end of particle growth. Regarding the nucleation time t_n, the Da number is in the order of magnitude $O(1)$ for the tests of high flow rates No.1. The slower mixing due to the lower flow rates in No.2 results in a high value of Da number, implying that when nucleation occurs, the fluid mixture is far from being homogeneous. In general, an extremely fast mixing can be reached in our microreator for the µSAS process with a mixing time of the order of magnitude of 10^{-5} s (0.01 ms). The same order of time is found for nucleation but much smaller than the global precipitation time. Consequently, these conditions are very favorable to precipitate, through µSAS conditions, the nanoparticles of TPE with a narrow particle size distribution.

CONCLUSION

In this paper, the experimental system to produce TPE nanoparticles by the μSAS process in our microreator was introduced. μSAS offers the possibility to obtain size under 15 nm. Narrow dispersion size (± 3 nm) was obtained. The variation of experimental parameters strongly impacts the hydrodynamics of the mixing. In particular, decreasing the flow rates increased the mean size of the recovered NPs. By comparing the simulation results to the experimental data, we have determined the solid-fluid interfacial tension σ, which is difficult to access by experimental measurements. The numerical model provided appropriate particle size d_p and size distribution, in good accordance with the experimental results. In order to have a deep insight in the mixing zone of the precipitation, some important fields have been analyzed numerically, namely: the mass fractions, the mixing time, the supersaturation and the mean particle size. The effects of fluid hydrodynamics on the particle size were discussed. At last, the characteristic times of precipitation and nucleation were determined, and compared to the mixing time measured under corresponding conditions in the microreactor. It has been demonstrated that the fluid mixing plays an essential role in μSAS precipitation and that our microreactor can offer an extremely fast mixing with a mixing time down to 0.01 ms, of the same order of magnitude as the nucleation time. This coupled experimental and numerical modeling approach highlights the high performance of the microreactor for fluid mixing and particle precipitation by μSAS process. It underlines the value of this technique for the controlled production of very small organic NPs, potentially paving the way of practical applications for a large number of organic compounds.

Acknowledgement

We acknowledge the French National Research Agency for its support (ANR-17-CE07-0029 - SUPERFON), the University of Bordeaux for the Ph.D. funding of the author Fan Zhang, the MCIA (Mésocentre de Calcul Intensif Aquitaine) and GENCI (DARI project number A0062A10815) for the HPC resources.

References

[1] W. Wani, M. Shahid, A. Hussain, M. Fahad AlAjmi, Fluorescent Organic Nanoparticles, Springer, Singapore, 2018.

[2] S. Fery-Forgues, Fluorescent organic nanocrystals and non-doped nanoparticles for biological applications, Nanoscale. 5 (2013) 8428. https://doi.org/10.1039/c3nr02657d.

[3] J. Zhang, Z. Xie, J. Zhang, J. Zhong, Nanosuspension drug delivery system: preparation, characterization, postproduction processing, dosage form, and application, Nanostructures Drug Deliv. E Andronescu Grumezescu Eds. (2017) 413–443.
[4] S. Kalepu, V. Nekkanti, Insoluble drug delivery strategies: review of recent advances and business prospects, Acta Pharm. Sin. B. 5 (2015) 442–453. https://doi.org/10.1016/j.apsb.2015.07.003.
[5] L. Padrela, M.A. Rodrigues, A. Duarte, A.M.A. Dias, M.E.M. Braga, H.C. de Sousa, Supercritical carbon dioxide-based technologies for the production of drug nanoparticles/nanocrystals – A comprehensive review, Adv. Drug Deliv. Rev. 131 (2018) 22–78. https://doi.org/10.1016/j.addr.2018.07.010.
[6] M. Li, M. Azad, R. Davé, E. Bilgili, Nanomilling of Drugs for Bioavailability Enhancement: A Holistic Formulation-Process Perspective, Pharmaceutics. 8 (2016) 17. https://doi.org/10.3390/pharmaceutics8020017.
[7] J.P. Möschwitzer, Drug nanocrystals in the commercial pharmaceutical development process, Int. J. Pharm. 453 (2013) 142–156. https://doi.org/10.1016/j.ijpharm.2012.09.034.
[8] H. Chen, C. Khemtong, X. Yang, X. Chang, J. Gao, Nanonization strategies for poorly water-soluble drugs, Drug Discov. Today. 16 (2011) 354–360. https://doi.org/10.1016/j.drudis.2010.02.009.
[9] A.A. Thorat, S.V. Dalvi, Liquid antisolvent precipitation and stabilization of nanoparticles of poorly water soluble drugs in aqueous suspensions: Recent developments and future perspective, Chem. Eng. J. 181–182 (2012) 1–34. https://doi.org/10.1016/j.cej.2011.12.044.
[10] V. Prosapio, E. Reverchon, I. De Marco, Formation of PVP/nimesulide microspheres by supercritical antisolvent coprecipitation, J. Supercrit. Fluids. 118 (2016) 19–26. https://doi.org/10.1016/j.supflu.2016.07.023.
[11] I.A. Cuadra, F. Zahran, D. Martín, A. Cabañas, C. Pando, Preparation of 5-fluorouracil microparticles and 5-fluorouracil/poly(l-lactide) composites by a supercritical CO2 antisolvent process, J. Supercrit. Fluids. 143 (2019) 64–71. https://doi.org/10.1016/j.supflu.2018.07.027.
[12] I. De Marco, M. Rossmann, V. Prosapio, E. Reverchon, A. Braeuer, Control of particle size, at micrometric and nanometric range, using supercritical antisolvent precipitation from solvent mixtures: Application to PVP, Chem. Eng. J. 273 (2015) 344–352. https://doi.org/10.1016/j.cej.2015.03.100.
[13] G. Bibi, Y. Jung, J.C. Lim, S.H. Kim, A Faster Approach to Stereocomplex Formation of High Molecular Weight Polylactide Using Supercritical Dimethyl Ether, Polym. Korea. 39 (2015) 453–460. https://doi.org/10.7317/pk.2015.39.3.453.
[14] L. Zhang, H. Nakamura, C. Lee, M. Uehara, H. Maeda, Determination of kinetic effects on particle size and concentration: instruction for scale up, IOP Conf. Ser. Mater. Sci. Eng. 18 (2011) 082027. https://doi.org/10.1088/1757-899X/18/8/082027.
[15] R. Couto, S. Chambon, C. Aymonier, E. Mignard, B. Pavageau, A. Erriguible, S. Marre, Microfluidic supercritical antisolvent continuous processing and direct spray-coating of poly(3-hexylthiophene) nanoparticles for OFET devices, Chem. Commun. 51 (2015) 1008–1011. https://doi.org/10.1039/C4CC07878K.
[16] F. Zhang, S. Marre, A. Erriguible, Mixing intensification under turbulent conditions in a high pressure microreactor, Chem. Eng. J. (2019) 122859. https://doi.org/10.1016/j.cej.2019.122859.
[17] J. Mei, N.L.C. Leung, R.T.K. Kwok, J.W.Y. Lam, B.Z. Tang, Aggregation-Induced Emission: Together We Shine, United We Soar!, Chem. Rev. 115 (2015) 11718–11940. https://doi.org/10.1021/acs.chemrev.5b00263.
[18] M. Champeau, J.-M. Thomassin, C. Jérôme, T. Tassaing, Solubility and Speciation of Ketoprofen and Aspirin in Supercritical CO_2 by Infrared Spectroscopy, J. Chem. Eng. Data. 61 (2016) 968–978. https://doi.org/10.1021/acs.jced.5b00812.
[19] P.J. Larkin, General Outline for IR and Raman Spectral Interpretation, in: Infrared Raman Spectrosc., Elsevier, 2018: pp. 135–151. https://doi.org/10.1016/B978-0-12-804162-8.00007-0.
[20] S. Foltran, E. Cloutet, H. Cramail, T. Tassaing, In situ FTIR investigation of the solubility and swelling of model epoxides in supercritical CO2, J. Supercrit. Fluids. 63 (2012) 52–58. https://doi.org/10.1016/j.supflu.2011.12.015.

[21] T. Onfroy, O. Marie, Determination of Integrated Molar Absorption Coefficients for Gaseous Phenol Infrared Bands and Influence of Water Vapor on Their Values, Am. J. Anal. Chem. 10 (2019) 9–22. https://doi.org/10.4236/ajac.2019.101002.
[22] J.-N. Ollagnier, T. Tassaing, S. Harrisson, M. Destarac, Application of online infrared spectroscopy to study the kinetics of precipitation polymerization of acrylic acid in supercritical carbon dioxide, React. Chem. Eng. 1 (2016) 372–378. https://doi.org/10.1039/C6RE00022C.
[23] S. Marre, A. Adamo, S. Basak, C. Aymonier, K.F. Jensen, Design and Packaging of Microreactors for High Pressure and High Temperature Applications, Ind. Eng. Chem. Res. 49 (2010) 11310–11320. https://doi.org/10.1021/ie101346u.
[24] A. Erriguible, T. Fadli, P. Subra-Paternault, A complete 3D simulation of a crystallization process induced by supercritical CO2 to predict particle size, Comput. Chem. Eng. 52 (2013) 1–9. https://doi.org/10.1016/j.compchemeng.2012.12.002.
[25] C. Neurohr, A. Erriguible, S. Laugier, P. Subra-Paternault, Challenge of the supercritical antisolvent technique SAS to prepare cocrystal-pure powders of naproxen-nicotinamide, Chem. Eng. J. 303 (2016) 238–251. https://doi.org/10.1016/j.cej.2016.05.129.
[26] J. Sierra-Pallares, D.L. Marchisio, M.T. Parra-Santos, J. García-Serna, F. Castro, M.J. Cocero, A computational fluid dynamics study of supercritical antisolvent precipitation: Mixing effects on particle size, AIChE J. 58 (2012) 385–398. https://doi.org/10.1002/aic.12594.
[27] S. Amiroudine, J.-P. Caltagirone, A. Erriguible, A Lagrangian–Eulerian compressible model for the trans-critical path of near-critical fluids, Int. J. Multiph. Flow. 59 (2014) 15–23. https://doi.org/10.1016/j.ijmultiphaseflow.2013.10.008.
[28] J. Im, W. Bae, J. Lee, H. Kim, Vapor−Liquid Equilibria of the Binary Carbon Dioxide−Tetrahydrofuran Mixture System, J. Chem. Eng. Data. 49 (2004) 35–37. https://doi.org/10.1021/je0202228.
[29] T. Voisin, A. Erriguible, G. Philippot, D. Ballenghien, D. Mateos, F. Cansell, B.B. Iversen, C. Aymonier, Investigation of the precipitation of Na2SO4 in supercritical water, Chem. Eng. Sci. 174 (2017) 268–276. https://doi.org/10.1016/j.ces.2017.09.009.
[30] C.R. Wilke, P. Chang, Correlation of diffusion coefficients in dilute solutions, AIChE J. 1 (1955) 264–270. https://doi.org/10.1002/aic.690010222.
[31] K. Goda, A multistep technique with implicit difference schemes for calculating two- or three-dimensional cavity flows, J. Comput. Phys. 30 (1979) 76–95. https://doi.org/10.1016/0021-9991(79)90088-3.
[32] P.L. Roe, Characteristic-Based Schemes for the Euler Equations, Annu. Rev. Fluid Mech. 18 (1986) 337–365. https://doi.org/10.1146/annurev.fl.18.010186.002005.
[33] J. Picot, S. Glockner, Reduction of the discretization stencil of direct forcing immersed boundary methods on rectangular cells: The ghost node shifting method, J. Comput. Phys. 364 (2018) 18–48. https://doi.org/10.1016/j.jcp.2018.02.047.
[34] J. Baldyga, J.R. Bourne, Simplification of micromixing calculations. I. Derivation and application of new model, Chem. Eng. J. 42 (1989) 83–92. https://doi.org/10.1016/0300-9467(89)85002-6.
[35] F. Zhang, A. Erriguible, S. Marre, Investigating laminar mixing in high pressure microfluidic systems, Chem. Eng. Sci. 205 (2019) 25–35. https://doi.org/10.1016/j.ces.2019.03.063.
[36] P.V. Danckwerts, The effect of incomplete mixing on homogeneous reactions, Chem. Eng. Sci. 8 (1958) 93–102. https://doi.org/10.1016/0009-2509(58)80040-8.
[37] A.D. Randolph, M.A. Larson, Theory of particulate processes: analysis and techniques of continuous crystallization, Academic Press, 1971.

Appendix

Hydrodynamic and thermodynamical contributions

The flow is considered as incompressible, monophasic and turbulent. As the simulation is performed down to the Kolmogorov scale, no turbulence model is needed, it reads:

$$\nabla \cdot \mathbf{u} = 0 \tag{6}$$

$$\rho\left(\frac{\partial \mathbf{u}}{\partial t} + \mathbf{u} \cdot \nabla \mathbf{u}\right) = -\nabla p + \nabla \cdot \mu\left[\nabla \mathbf{u} + \nabla^{t} \mathbf{u}\right] \tag{7}$$

in which p is the pressure, ρ the density of the fluid, g the gravity vector, μ the dynamic viscosity, t the time and **u** the velocity vector. The Peng Robinson equation of state (PR-EOS) with quadratic mixing rules is chosen to calculate the density of the fluid.
The species continuity equations are expressed by taking into account the diffusion of species according to the Fick's law:

$$\rho \frac{\partial \omega_a}{\partial t} + \nabla \cdot \left(\rho \omega_a \mathbf{u} - \rho D_a \nabla \omega_a\right) = 0 \tag{8}$$

$$\rho \frac{\partial \omega_s}{\partial t} + \nabla \cdot \left(\rho \omega_s \mathbf{u} - \rho D_s \nabla \omega_s\right) = -3\rho_p k_v G m_2 \tag{9}$$

with ω_a and ω_s the mass fractions of solvent and solute, respectively, D_a and D_s the diffusion coefficients of solvent and solute in solvent/CO_2, respectively. ρ_p is the density of the solid solute and k_v the volume shape factor of the particles that is based on the morphology of produced particles (k_v = p/6).

The population balance equation

As in our case, the precipitated particles obtained experimentally in the microreactor are very small, we assume that the effect of the breakage and the agglomeration can be neglected. According to the conservation law, the general equation of population balance is defined by:

$$\rho \frac{\partial n(L, X, t)}{\partial t} + \nabla \cdot \left(\rho \mathbf{u} n(L, X, t)\right) + \rho \frac{\partial n(L, X, t) G}{\partial L} = 0 \tag{10}$$

In this equation n represents the number density function which depends on internal coordinates (particle size L) and external coordinates (space coordinates X (x,y,z)). u and ρ are respectively the velocity and the density of the fluid and G is the growth rate of the particles. The population balance equation is solved with the standard method of moments. Only the four first moments are solved, the system of equations to be solved remains [37]:

$$\rho \frac{\partial m_j}{\partial t} + \nabla \cdot \left(\rho \bar{\mathbf{u}} m_j\right) = \rho\left(0^j B + jGm_{j-1}\right) \qquad for\ j = 0,1,2,3 \tag{11}$$

where m_j is the j^{th} moment defined by:

$$m_j = \int_0^{\infty} n(L, X, t) L^j dL$$

where m_j is the j^{th} moment of the distribution. B and G represent the nucleation and the growth rates.
Assuming that the distribution is log-normal, the following relationship [37] is used to build the simulated particle size distribution with the calculated moments:

$$N(L) = \frac{1}{L\ln(\sigma)\sqrt{2\pi}}\left(\frac{-\ln^2\left(\frac{L}{\overline{L}}\right)}{2\ln^2(\sigma)}\right) \quad \text{with} \quad \ln^2(\sigma) = \ln\left(\frac{m_0 m_2}{m_1}\right) \tag{12}$$

Nucleation and Growth parameters

We consider that particle formation is only due to primary nucleation:

$$B = 1.5 D_{wc}\left(C_{sat} S N_a\right)^{7/3}\sqrt{\frac{\sigma}{k_b T}} V_m \, exp\left(-\frac{16\pi}{3}\left[\frac{\sigma}{k_b T}\right]^3 \frac{V_m^2}{ln^2(S)}\right) \tag{13}$$

with N_a the Avogadro constant, σ the solid-fluid interfacial tension, k_b the Boltzmann constant and V_m the solute molecular volume, D_{WC} the solute diffusion coefficient calculated by the correlation proposed by Wilke and Chang (1955).
The growth rate, assuming that the main mechanism for growth is diffusion, is calculated by:

$$G = k_g C_{sat}(S - 1) \tag{14}$$

where k_g represents the mass transfer coefficient deduced of the local Sherwood number. This one is estimated by the Froessling equation.

Nomenclature

B	nucleation rate ($1/(m^3 s)$)
C	concentration (mol/m^3)
D	diffusion coefficient (m^2/s)
g	gravity vector (m/s^2)
G	growth rate (m/s)
K_b	Boltzmann constant ($m^2\ kg\ s^{-1}\ K^{-1}$)
k_g	mass transfer coefficient ($m^4/(mol.s)$)
L	length of the particles (m)
m_k	k^{th} order moment (m^k/m^3)
n	particles density function ($1/m^3$)
Na	Avogadro number (1/mol)
p	pressure (Pa)
S	supersaturation
T	temperature (K)
t	time (s)
u	velocity vector (m/s)
V_m	molecular volume (m^3)

Greek letters

μ	viscosity (Pa.s)
σ	surface tension (N/m)
ρ	density (kg/m^3)
ω	mass fraction